Article

Structure

# The Neuronal Migration Factor srGAP2 Achieves Specificity in Ligand Binding through a Two-Component Molecular Mechanism

## Graphical Abstract

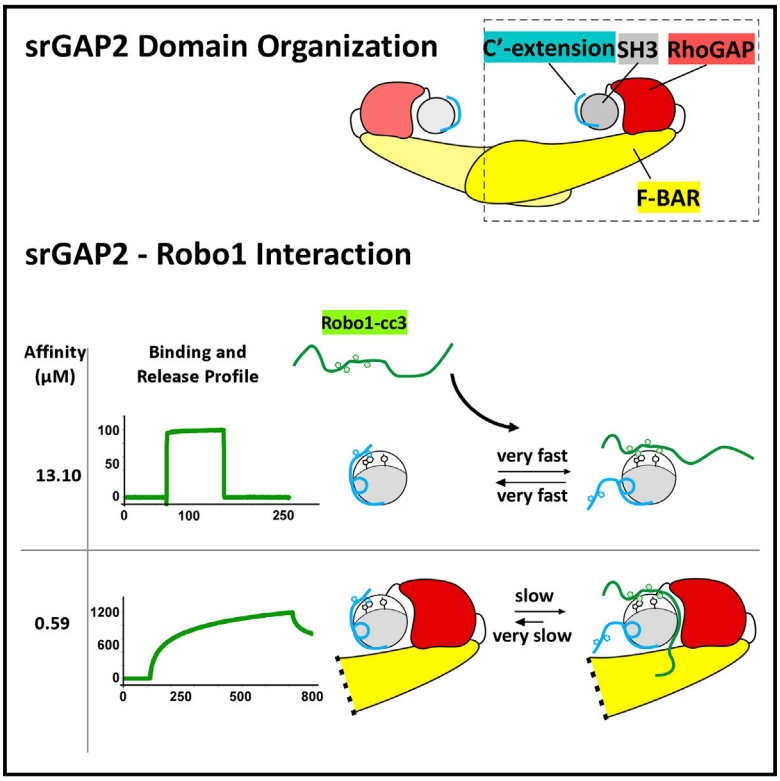


## Highlights

- The srGAPs' SH3 domain is necessary but not sufficient for effective ligand binding
- Effective ligand binding requires the larger F-BAR-RhoGAP-SH3 srGAP module
- Ligand binding to srGAP2 is moderately autoinhibited by an SH3 carboxy (C′) extension
- The SH3 carboxy (C′) extension utilizes polyproline mimicry and binds in *cis* or *trans*

## Authors

Julia Guez-Haddad, Michael Sporny, Yehezkel Sasson, ..., David Margulies, Jens Radzimanowski, Yarden Opatowsky

## Correspondence

yarden.opatowsky@biu.ac.il

## In Brief

srGAP proteins regulate cell migration and morphogenesis by shaping the structure and dynamics of the cytoskeleton and membranes. Guez-Haddad et al. reveal two structural determinants that allow srGAPs to be recruited and placed accurately at their signaling sites.

Guez-Haddad et al., 2015, Structure *23*, 1989–2000
November 3, 2015 
http://dx.doi.org/10.1016/j.str.2015.08.009

Structure
Article

# The Neuronal Migration Factor srGAP2 Achieves Specificity in Ligand Binding through a Two-Component Molecular Mechanism

Julia Guez-Haddad,[1] Michael Sporny,[1] Yehezkel Sasson,[2] Lada Gevorkyan-Airapetov,[1] Naama Lahav-Mankovski,[3] David Margulies,[3] Jens Radzimanowski,[4] and Yarden Opatowsky[1,*]
[1]The Mina & Everard Goodman Faculty of Life Sciences, Bar-Ilan University, Ramat Gan 5290002, Israel
[2]Biolojic Design Ltd., Ramat Gan 5290002, Israel
[3]Department of Organic Chemistry, Weizmann Institute of Science, 7610001 Rehovot, Israel
[4]Unit of Virus Host-Cell Interactions, UJF-EMBL-CNRS, 38042 Grenoble, France
*Correspondence: yarden.opatowsky@biu.ac.il
http://dx.doi.org/10.1016/j.str.2015.08.009

## SUMMARY

**srGAP proteins regulate cell migration and morphogenesis by shaping the structure and dynamics of the cytoskeleton and membranes. First discovered as intracellular effectors for the Robo1 axon-guidance receptor, srGAPs were later identified as interacting with several other nuclear and cytoplasmic proteins. In all these cases, the srGAP SH3 domain mediates protein-protein interactions by recognizing a short proline-rich segment on the cognate-binding partner. However, as interactions between the isolated SH3 domain and a selected set of ligands show weak affinity and low specificity, it is not clear how srGAPs are precisely recruited to their signaling sites. Here, we report a two-component molecular mechanism that regulates ligand binding to srGAP2 by on the one hand dramatically tightening their association and on the other, moderately autoinhibiting and restricting binding. Our results allow the design of point mutations for better probing of srGAP2 activities, and may facilitate the identification of new srGAP2 ligands.**

## INTRODUCTION

The four human Slit-Robo GTPase-activating proteins (srGAPs) control the migration and morphology of cells by coupling and coordinating remodeling reactions of the plasma membrane and the actin-based cytoskeleton. srGAPs accomplish this complex task through a unique domain composition of an extended F-BAR, followed by RhoGAP and SH3 domains that mediate membrane association and deformation, cytoskeleton remodeling, and protein-protein interactions, respectively (Guerrier et al., 2009). A possible mechanism of action of srGAP proteins was presented for srGAP3 (Endris et al., 2011), whereby srGAP3 recruitment to leading edges of cellular lamellipodia and focal adhesions relies on the association of both the F-BAR and SH3 domains with protruding membranes and lamellipodia-specific proteins. The accurate subcellular localization of srGAP3 allows its RhoGAP domain to effectively inactivate the small GTPase Rac1, which, in turn, leads to WAVE1 downregulation, the subsequent breakdown of local actin cytoskeleton structures, and the retraction of membrane protrusions. This mechanism portrays srGAPs as proteins that are recruited to protruding cellular sites to restrict further expansion. The functions of F-BAR (FES-CIP4 homology) domains, as well as those of the other members of the BAR superfamily (i.e., BAR [Bin/amphiphysin/RVS], I-BAR [inverse BAR], and N-BAR [N-terminal BAR] domains), are directly linked to their three-dimensional (3D) structure and oligomeric organization. They all form membrane-binding dimers that can induce and/or stabilize membrane curvatures. The radius and direction of the membrane curvature (whether related to cellular invagination, evagination, or flat surfaces) is correlated to the molecular curvature of the membrane-binding surface of the BAR dimer and the oligomeric arrangement of the BAR dimers in a larger assembly of membrane-associated lattices (Frost et al., 2009). Indeed, the F-BAR domains of srGAP proteins were shown to induce membrane protrusions. Most notably, the F-BAR domain of srGAP2 induces tubular membrane protrusions in vitro, in COS-7 cells and primary neuronal cell cultures, and endogenous srGAP2 was detected in subcellular sites distinguished by outward membrane protrusions, i.e., dendritic spines and axonal growth cones (Carlson et al., 2011; Coutinho-Budd et al., 2012; Guerrier et al., 2009; Yamazaki et al., 2013; Yao et al., 2008).

srGAP proteins, like many other BAR superfamily members, also include an SH3 domain that coordinates their localization and activity with other signaling molecules and cytoskeleton effectors (Qualmann et al., 2011). Accordingly, srGAP proteins were initially discovered in a yeast two-hybrid screen as cytoplasmic effectors of the Robo1 axon-guidance receptor, where a specific proline-rich cytoplasmic segment of Robo1, termed cc3, was shown to mediate binding to the SH3 domain of srGAP1, 2, and 3, while the rest of the Robo1 intracellular domain, including the proline-rich cc2 segment, did not bind to the srGAPs (Wong et al., 2001). However, later in vitro studies that investigated srGAP2 interactions did not provide further convincing corroboration for the Robo1-srGAP2 interaction. One study that measured direct SPR (surface plasmon resonance) interactions between synthetic Robo1-cc3 peptides of various lengths and

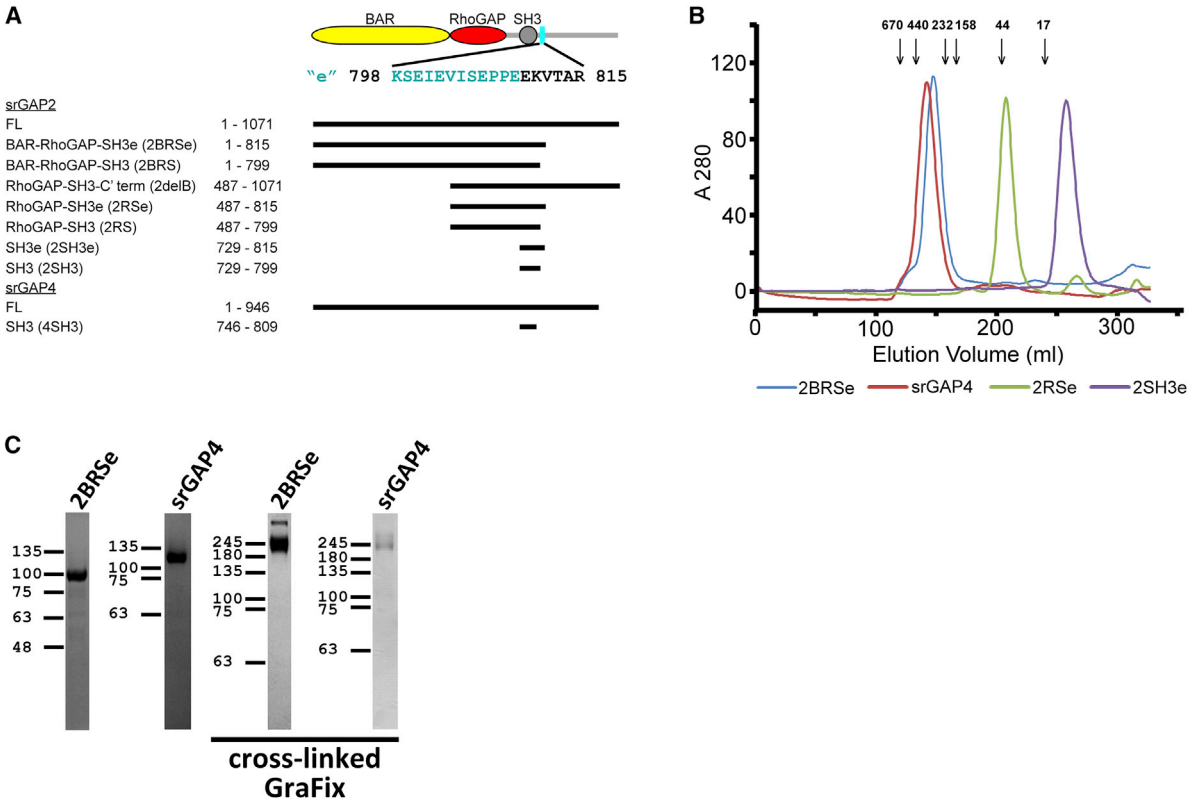


**Figure 1. Domain Organization and Dimerization of srGAP Proteins**

(A) Human srGAP2, srGAP4, and srGAP2 deletion mutants used in this study. In the scheme the F-BAR, RhoGAP, and SH3 domains are indicated and appear as colored shapes. The SH3 C′ extension is colored cyan.

(B and C) Size-exclusion chromatography by Superdex 200 26/60 (standard molecular weights indicated) (B) and cross-linking by glutaraldehyde gradient fixation (GraFix) analyzed by SDS-PAGE (C) of purified srGAP2 and srGAP4 demonstrate F-BAR-dependent dimerization of srGAP proteins, while the 2SH3e and 2RSe constructs that lack the F-BAR domain are eluted as monomers.

the isolated SH3 domains of srGAP1, 2, and 3 did not detect binding with most peptides and only a weak and transient interaction (apparent $K_D$ of ~5 μM) with one peptide (Li et al., 2006). A different study that used photo-trapping to capture weak binding partners for the SH3 domains of srGAP2 and srGAP4 (ARHGAP4) did not report Robo1 as one of the identified ligands (Okada et al., 2013). Instead, several other proline-rich proteins, e.g., the postsynaptic scaffolding protein Gephyrin and the nuclear telomerase regulator YLPM1, were detected. These join a growing list of other putative srGAP effectors, such as the cytoskeletal organization protein formin (Mason et al., 2011) and the scaffolding protein WAVE-1 (Soderling et al., 2007), which were found to interact and act through srGAP2 and srGAP3.

If, indeed, srGAPs bind so weakly to Robo1 while also being capable of interacting with a large repertoire of potentially competing partners, how can miswiring be avoided and accurate signaling axes formed? In this study, we address these questions by studying the molecular basis for protein-protein interactions by srGAP2 using SH3-binding segments from three different proteins (Robo1, Gephyrin, and YLPM1). Our investigations revealed an integrated two-component mechanism that provides much stronger affinity and specificity to certain binding partners. This is achieved by the cooperative involvement of the F-BAR and RhoGAP domains in SH3 interactions, while restricting ligand access through an autoinhibitory switch that is sensitive to the local concentration of srGAP2.

Taken together, our results will allow the identification of genuine srGAP-binding partners in future screens by using the F-BAR-RhoGAP-SH3 module instead of the isolated SH3 domain, and strongly support the existence of a Robo1-srGAP signaling axis. Also, this study reveals an SH3 carboxy extension segment that, depending on srGAP2 concentration, can bind to the SH3 domain in *cis*, or to a neighboring srGAP2 molecule in *trans.* Thus, the SH3 carboxy extension might actually serve two different purposes: preventing the binding of non-specific ligands, and mediating intermolecular contacts in the srGAP2 membrane-associated lattice.

## RESULTS

### Limited Proteolysis Analysis of srGAP2 Reveals a Stable SH3 Carboxy Extension

We used *Escherichia coli* for the recombinant expression of human srGAP proteins. As expected, gel-filtration and gradient fixation analyses showed that srGAP2 and srGAP4 are dimers in solution, consistent with F-BAR-domain-mediated dimerization (Figures 1 and S1). Using limited trypsin digestion followed by liquid chromatography-electrospray ionization-mass

**Table 1. Crystallographic Statistics**

| Data Collection Statistics | | |
|---|---|---|
| Beamline (ESRF) | ID-29 | ID-29 |
| Wavelength (Å) | 0.976 | 0.976 |
| Space group | $P2_12_12_1$ | $P2_1$ |
| Unit cell parameters (Å) | *a* = 31.30, *b* = 52.54, *c* = 92.51 | *a* = 49.51, *b* = 31.35, *c* = 62.83; β = 113.07° |
| Total reflections[a] | 59,638 (4,560) | 98,309 (9,190) |
| Unique reflections[a] | 12,959 (1,177) | 15,014 (1,410) |
| Completeness (%)[a] | 98.4 (91.2) | 97.13 (95.01) |
| $R_{meas}$ (%)[a,b] | 11.6 (60.6) | 11.37 (67.2) |
| Mean $I/\sigma$[a] | 10.77 (2.11) | 10.55 (3.06) |
| Resolution range (Å) | 46.26–1.87 | 57.81–1.73 |
| $CC_{1/2}$[a] | 0.99 (0.86) | 0.99 (0.93) |
| Refinement Statistics | | |
| $R_{work}$ (%)[a] | 0.22 (0.36) | 0.18 (0.24) |
| $R_{free}$ (%)[a] | 0.25 (0.37) | 0.22 (0.24) |
| No. of non-hydrogen atoms | 1,366 | 1,427 |
| Macromolecules | 1,280 | 1,317 |
| Water | 71 | 110 |
| Protein residues | 160 | 167 |
| Root-mean-square (bonds) | 0.013 | 0.015 |
| Root-mean-square (angles) | 1.56 | 1.61 |
| Ramachandran favored (%) | 99 | 97 |
| Ramachandran outliers (%) | 0 | 1.2 |
| Clashscore | 1.97 | 2.71 |
| Average B factor | 34.00 | 27.9 |
| RCBS PDB code | 4RTT | 4RUG |

[a]Values of the highest-resolution shell are given in parentheses.
[b]$R_{meas} = \Sigma_h[m/(m-1)]^{1/2}\,\Sigma_i|I_{h,i} - \langle I_h\rangle|/\Sigma_h\Sigma_i I_{h,i}$.

spectrometry analysis, we probed the structural features of srGAP2 by identifying sites with enhanced backbone flexibility. The most prominent protein fragment (497 KQDS....VTAR 815) that resisted a 20-hr digestion period spans the RhoGAP and SH3 domains, with a carboxy extension of 30 residues (Figure S1). This extension (786 DTEDGVVERSSPKSEIEVISEPPEEKVTAR 815), which harbors three putative trypsin digestion sites (… ER$^{v}$S … PK$^{v}$S … EK$^{v}$V …), is predicted to have a disordered secondary structure; therefore, its resistance to overnight digestion was unexpected.

## Crystal Structure of srGAP2 SH3e

Our limited proteolysis analysis suggested that the SH3 carboxy extension forms close contacts with the RhoGAP-SH3 domains. To reveal the nature of these interactions, we pursued high-resolution structural information, and were able to crystallize the 2SH3e construct (which stands for srGAP2 SH3, carboxy extension) (Figure 1A) and determine its 3D X-ray structure. Crystals of two space groups (P2 and $P2_12_12_1$) were obtained and diffracted to maximal resolutions of 1.73 and 1.87 Å, respectively (Table 1). In both cases, two protein copies occupied one asymmetric unit (Figure S2).

The general topology of the 2SH3e core domain is very similar to those of several other SH3 domains, including p40phox and c-Crk, which have available crystal structures in a complex with polyproline ligands (PDB: 1W70 and 1CKA). The SH3 core domain (residues P730–Q785) has five β strands (β1–β5) arranged as two antiparallel sheets, giving rise to a β-barrel fold. The RT, N-Src, and distal loops connect the β1-β2, β2-β3, and β3-β4 strands, respectively, while a short helix connects β4 and β5 (Figure 2).

In most cases, SH3 (Src-homology 3) domains recognize ligands that present a PxxP minimal consensus sequence, where each proline binds to a reciprocal "Px" and "xP" hydrophobic "pocket" on the SH3 surface that, together, constitute the "PxxP binding groove." In some cases, additional binding sites on the target SH3 surface (located outside the PxxP binding groove), such as the "specificity pocket" and the "specificity zone," are also utilized (Zarrinpar et al., 2003). Based on a comparison to the p40phox and c-Crk crystal structures, we assigned these clefts to the 2SH3e structure and identified tyrosine 781, tryptophan 765, and glutamate 746 to be key residues in the Px, xP, and specificity pocket clefts, respectively (Figure 2).

Twenty-four of the carboxy extension residues, D786–E809, are visible in the structure, and are subdivided into two segments; each includes a short helix flanked by loop connectives. The first segment, which spans residues D786–P797, forms close *cis* interactions, while the second segment (K798–E809) interacts in *trans* with a symmetry-mate molecule, and is henceforth referred to as the SH3 C′ extension and by an "e" in the construct acronyms. The C′-extension binding surface on the symmetry-mate molecule spans the xP binding cleft and extends to the specificity zone (Figures 2 and 3 and Figure S3). Three C′-extension residues (E800, V803, and I804) are located on one face of a short helix (E800–S805) that directly interacts with the specificity zone through hydrophobic and polar contact. The four residues at the carboxy end of the C′ extension 806 EPPE 809 bind to the SH3 xP binding cleft in the same way that polyproline ligands do. Most notably, P807 assumes a backbone carbonyl position that forms a hydrogen bond with the indole secondary amine of W765, thereby mimicking a canonical Pxx**P** proline ligand position and function (Figures 2 and 3). As P807 is conserved in srGAP2 paralogs and orthologs of most chordate creatures, the possible functionality and interactions of this residue are further emphasized. The similarity to canonical SH3 polyproline ligands led us to view the C′ extension as a part of an autoinhibitory mechanism aimed at restricting protein binding to srGAP2.

## C′-Extension Binding and Secondary Structure

We generated additional constructs of srGAP proteins that have or lack the SH3 C′ extension: (1) 2BRSe (which stands for srGAP2 F-BAR, RhoGAP, SH3, C′ extension) srGAP2, which is truncated after the SH3 C′ extension; (2) 2BRS; (3) 2delB (srGAP2, which lacks the F-BAR); (4) 2RSe; (5) 2RS; (6) 2SH3; and (7) 4SH3 (SH3 of srGAP4). These constructs were successfully expressed in *E. coli* and purified, exhibiting high protein stability and homogeneity, as evaluated by size-exclusion chromatography analysis. As expected, 2BRS and 2BRSe are dimers, based on gradient fixation analysis, while the constructs lacking the F-BAR domain are monomeric (Figure 1).

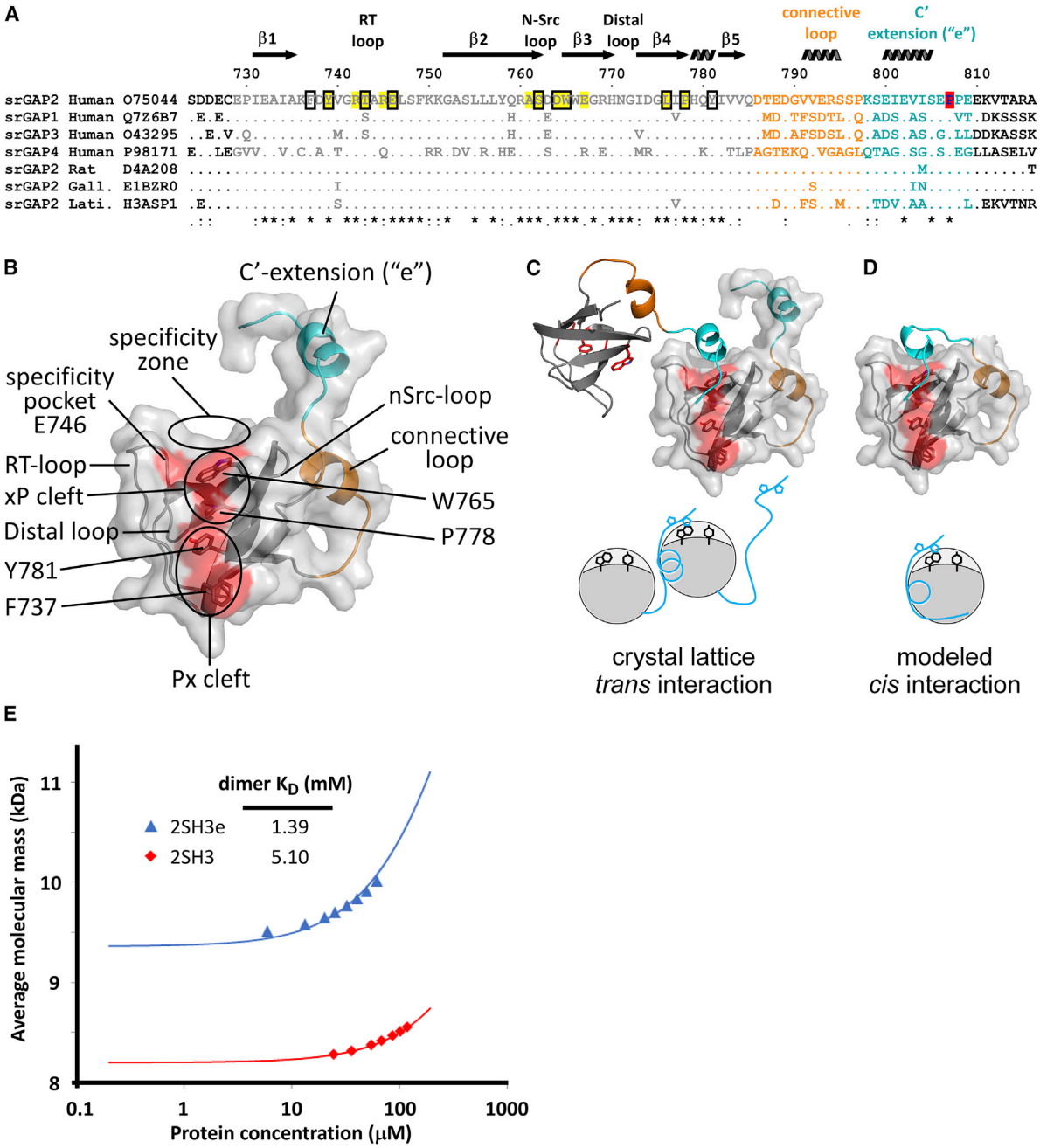


**Figure 2. Crystal Structure, Autoinhibition, and Dimerization of the srGAP2 SH3 Domain**

(A) Sequence alignment and structural features of the srGAP2 SH3 domain region. Sequences of human srGAP2 orthologs and paralogs were manually aligned and secondary structure elements assigned. Gray letters represent the SH3 core region, orange and cyan represent the connective loop and C′ extension, respectively, and sequence identity is marked by dots. The residues involved in *trans* interaction with neighboring C′ extension are highlighted in yellow, and residues involved with polyproline recognition in canonical SH3 domains are boxed in black, as represented by c-Crk standard structure (PDB: 1CKA). The key proline 807 is highlighted in red.

(B) Ribbon and surface representation of the extended srGAP2 SH3 (2SH3e) determined at 1.73 Å resolution. The SH3 core and C′ extension are colored as in (A) with gray and cyan, respectively. The canonical polyproline binding groove surface is highlighted in red, and the Px, xP, specificity zone, and specificity pocket are labeled.

(C) A crystallographic symmetry-related dimer of 2SH3e shows how one molecule’s C′ extension docks onto the specificity and xP pockets of a neighbor 2SH3e molecule. A simplified illustration of the 2SH3e dimer portrays the PxxP binding groove as a light-gray crescent, with Y781 (Px pocket) and W765 (xP pocket) appearing as sticks. The C′ extension (cyan coil) of the “donor” molecule binds to a neighbor “acceptor” molecule, while the C′ extension of the acceptor cannot reach the binding site on the donor and, therefore, appears unfolded in a dimer.

(D) Modeled C′-extension binding in *cis*. The C′ extension can reach the specificity zone and xP pocket at the expense of several atomic interactions that exist in the *trans* interaction.

*(legend continued on next page)*

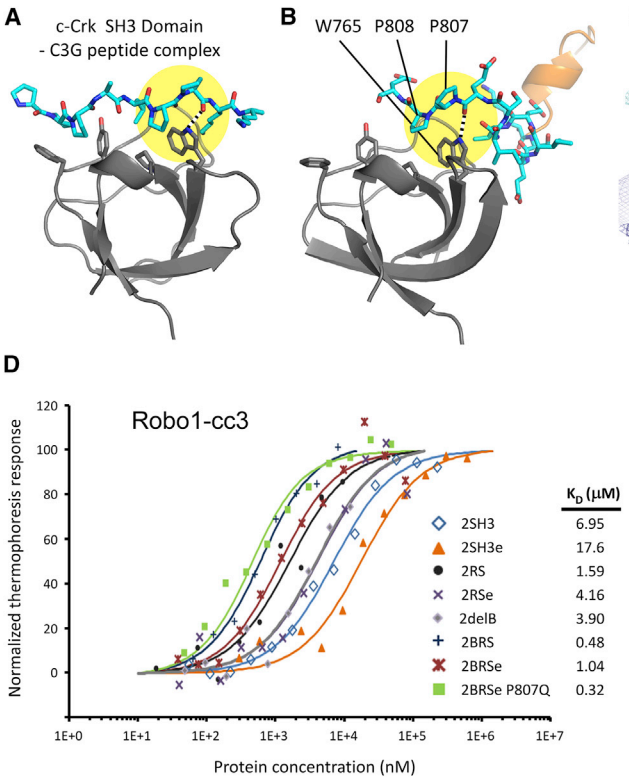


**Figure 3. The C′ Extension Utilizes Polyproline Mimicry to Inhibit Protein Binding to srGAP2**

(A) The crystal structure of c-Crk (p38) N-terminal SH3 domain (PDB 1CKA) with C3G peptide presents a "canonical" SH3-polyproline complex. The yellow circle highlights the xP pocket tryptophan and its association with the C3G peptide proline residues.

(B) The crystal structure of 2SH3e with the same orientation as (A) reveals how the C′ extension (cyan) mimics a polyproline ligand. Note how prolines 807 and 808 assume positions similar to that of the C3G ligand of the c-Crk structure.

(C) A $2F_o$-$F_c$ electron density map contoured to 1.3σ, focusing on the xP pocket site and with the same orientation and color code as in (B).

(D) Microscale thermophoresis (MST) titration curves and apparent $K_D$ values for Robo1-cc3 binding to srGAP2 constructs. Measured thermophoresis values (symbols) fitted to a one-to-one binding model (solid lines). Binding is strongest to the 2BRS and weakest to the 2SH3 constructs. Note that for all constructs, the C′ extension moderately inhibits binding, and that the point mutation P807E abolishes the inhibitory effect.

In both the orthorhombic and monoclinic crystal lattices of 2SH3e, the C′ extension interacts in *trans* with the SH3 core of a symmetry-mate molecule. We investigated whether this *trans* interaction also occurs in solution, and used CG-MALS (composition-gradient multi-angle static light scattering) to compare the oligomeric state of 2SH3e with that of 2SH3. The results show that while both proteins are virtually monomeric at concentrations of up to 10 μM, 2SH3e has about 10% dimeric fraction at 100 μM and a calculated dimerization dissociation constant of 1.39 mM. By contrast, 2SH3, which lacks the C′ extension, has a much weaker dimerization constant of 5.1 mM (Figure 2). Next, we considered whether the C′ extension can also bind in *cis*. Superimposing the C′ extension to the *cis* position shows that such a conformation is sterically possible (Figure 2) at the expense of altering the positions of two residues: K799 and E800. Based on this analysis, we conclude that while a C′-extension interaction in *cis* is possible, a *trans* interaction may be more favorable, especially at high local concentration conditions of srGAP2. It is important to note that in the context of a dimeric interaction, where the C′ extension of a "donor" molecule binds in *trans* to an "acceptor" molecule, the short length of the C′ extension and its spatial arrangement prevent the C′ extension of the acceptor to reach the binding site on the donor, which would leave the donor unbound and fully exposed (Figure 2).

We next calculated the binding affinity of a synthesized C′-extension peptide to 2SH3 using intrinsic tryptophan fluorescence intensity measurements, which are particularly useful in our case because the bound C′ extension occludes the only tryptophan (W765) of 2SH3e that is surface exposed (Figures 2 and 3). By titering increasing concentrations of a C′-extension peptide (gcggKSEIEVISEPPEEKVT-813) to 2SH3 that was maintained at a steady 6 μM concentration, we calculated an apparent dissociation constant of 1.2 ± 0.4 mM (Figure S4). This $K_D$ value is very similar to the 2SH3e dimerization dissociation constant of 1.39 mM that we measured using GC-MALS.

We next considered whether, like other characterized autoinhibitory segments, the C′ extension also undergoes an induced helical transition upon interaction with its cognate-binding surface. The crystallographic data show that a portion of the C′ extension has a helical conformation in the crystal, in contrast to its predicted random-coil secondary structure. To test whether this segment assumes a random-coil structure when isolated, we measured a circular dichroism (CD) spectrum of the C′-extension peptide in water. A second CD measurement, in 40% trifluoroethanol (TFE) solution that induces hydrogen bond formation, was conducted to determine the potential helicity content of the peptide (Figure S5), as we previously demonstrated (Opatowsky et al., 2004). Deconvolution of the CD spectra (Greenfield, 2006) shows an all-coil structure in water while having a 20% α-helicity in the mixed water/TFE solution,

(E) 2SH3e dimerization in solution is mediated by the C′ extension. Different concentrations of 2SH3 and 2SH3e were measured by composite-gradient multi-angle light scattering (CG-MALS). The weight average molar masses were plotted as a function of concentration (dots on the graph). Each data point represents the average molecular weight of the relevant concentration measured via the Calypso system, together with MALS apparatus and a refractive index detector. Each dataset is fitted with a nonlinear regression to a model of monomer-dimer equilibrium (solid line). Dimerization constants ($K_D$) calculated by nonlinear regression fit are indicated for each protein.

**Table 2. Kinetic Parameters**

**Microscale Thermophoresis Measurements: Apparent $K_D$ Values in μM**

| srGAP2 Construct | Robo1 cc3 | Gephyrin | YLPM1 | Robo1 cc2 |
|---|---|---|---|---|
| 2SH3 | 6.95 ± 0.271 | 22.6 ± 1.58 | 2.53 ± 0.08 | |
| 2SH3e | 17.60 ± 1.21 | 40.90 ± 3.22 | 9.28 ± 0.61 | |
| 2RS | 1.59 ± 0.14 | | | |
| 2RSe | 4.16 ± 0.30 | | | |
| 2delB | 3.9 ± 0.2 | | | |
| 2BRS | 0.48 ± 0.01 | 0.712 ± 0.03 | 2.09 ± 0.1 | 41.40 ± 1.16 |
| 2BRSe | 1.04 ± 0.05 | 3.170 ± 0.21 | 3.02 ± 0.13 | NA |
| 2BRSe P807Q | 0.32 ± 0.02 | 0.80 ± 0.04 | 1.54 ± 0.12 | |

**Surface Plasmon Resonance: Robo1 cc3 Binding Kinetics**

| srGAP Construct | $K_D$ (μM) | $k_{on}$ ($M^{-1}·s^{-1}$) | $k_{off}$ ($s^{-1}$) | $\chi^2$ ($RU^2$) |
|---|---|---|---|---|
| 2SH3 | 6.19 | 196,000 | 2.57 | 2.48 |
| 2SH3e | 13.10 | 333,000 | 2.06 | 3.62 |
| 2RS | 1.15 | 330.3 | 0.00038 | 3.28 |
| 2RSe | 4.49 | 398.8 | 0.00177 | 0.34 |
| 2BRS | 0.22 | 4,560 | 0.00100 | 0.43 |
| 2BRSe | 0.59 | 5,480 | 0.00325 | 10.3 |
| 4SH3 | 7.65 | 231,000 | 1.769 | 7.24 |
| srGAP4 | 0.34 | 16,200 | 0.00553 | 12.5 |

which corresponds exactly to the helical fraction of the C′ extension, as seen in the crystal structure. This implies that the C′ extension undergoes a coil-to-helix transition during its association with the SH3 specificity zone.

## The C′ Extension Inhibits Protein Binding to 2SH3e

We next measured the inhibitory effect that the C′ extension imparts on the binding of srGAP2 to Robo1, Gephyrin, and YLPM1. For these measurements, we used 23-residue-long synthesized peptides that we N′-labeled with biotin and fluorescein. These peptides correspond to the Robo1-cc3, Gephyrin E-domain, and YLPM1 peptides (Figure S6). To measure the binding affinities, we used microscale thermophoresis (MST) for all three peptides and SPR only for Robo1-cc3; the summarized results are presented in Table 2. All three peptides show 1.8- to 3.1-fold weaker $K_D$ values for 2SH3e association in comparison with 2SH3, thereby demonstrating the autoinhibitory role of the C′ extension (Figures 3 and S7). For all three peptides, binding affinities to 2SH3e and 2SH3 were weak. For example, Robo1-cc3 binds 2SH3 and 2SH3e with $K_D$ of 6.9 and 17.6 μM, respectively, as determined by MST. SPR measurements of Robo1-cc3 were consistent with the MST results, with $K_D$ of 6.19 and 13.1 μM for 2SH3 and 2SH3e, respectively (Table 2). The SPR binding and release profile presents very rapid $k_{on}$ (3.33E+05 and 1.96E+05 [$M^{-1}$ $s^{-1}$]) and $k_{off}$ (2.06 and 2.57 [$s^{-1}$]) values for Robo1-cc3 binding to 2SH3 and 2SH3e, respectively (Table 2; Figures 2 and S7).

## The F-BAR and RhoGAP Domains Modulate Binding Kinetics

We also measured the binding affinities of the Robo1-cc3, Gephyrin, and YLPM1 peptides to larger srGAP2 constructs (Figure 1A). As in the case of binding to the SH3 domain, all the peptides showed weaker affinities for constructs that include the C′ extension, further confirming its role in the autoinhibition of ligand binding (Table 2; Figures 3 and S7). Also, it is clear that the C′ extension alone restricts ligand binding to srGAP2, since a construct that includes the entire carboxy terminal tail (2delB) showed very similar Robo1-cc3 binding, as did a construct (2RSe) lacking the long C′ tail.

Comparison of the $K_D$ values obtained for 2SH3 with those obtained for 2BRS revealed remarkably stronger Robo1-cc3 and Gephyrin binding to the 2BRS constructs. The differences in $K_D$ are not exactly the same for Robo1-cc3 and Gephyrin, and range between a 13- and 33-fold increase in affinity, depending on peptide, method of measurement (MST versus SPR), and whether the srGAP2 construct has or lacks the C′ extension. Unlike Robo1-cc3 and Gephyrin, only a mere 1.25- to 3-fold increase in affinity was observed for YLPM1. Analysis of the SPR measurements of Robo1-cc3 interaction with the 2BRS constructs revealed completely different binding and release kinetics compared with those of the 2SH3 constructs, where the 2SH3 constructs had about 100-times faster on-rates and 1,000-times faster off-rates than the 2BRS constructs (Table 2 and Figure 4). We also measured and compared the binding kinetics of Robo1-cc3 to 4SH3 and srGAP4. The results were very similar to those obtained for srGAP2, with weak (7.6 μM) versus strong (0.34 μM) $K_D$ values for Robo1-cc3 binding to 4SH3 and srGAP4, respectively (Table 2, determined by SPR). Also, the binding and release kinetic profiles of 4SH3 and srGAP4 were similar to those of 2SH3 and 2BRS, demonstrating fast versus slow interaction rates (Figure S7). These results prove that the F-BAR and RhoGAP domains have a dramatic impact on the binding kinetics of some ligands to srGAP2 and srGAP4, facilitating relatively strong (submicromolar) interactions.

We further inquired what might be the specific roles of the F-BAR and RhoGAP domains in modulating ligand binding to srGAP2. To this end, we used SPR to measure the binding kinetics of Robo1-cc3 to 2RSe and 2RS. We found that while the off-rates for 2RS constructs are very similar to those for 2BRS (and slower than those for 2SH3), the on-rates are about ten times slower, resulting in overall weaker binding affinities in comparison with those of the 2BRS constructs (Table 2 and Figure 4). A possible interpretation of these results is that the F-BAR domain stabilizes the RhoGAP-SH3 interdomain orientation, which would otherwise be more flexible. The stabilized RhoGAP-SH3 module forms an elaborate binding surface that binds ligands stronger and slower than the isolated 2SH3.

## The SH3 Domain of srGAP2 Is, Nevertheless, Necessary for Robo1-cc3 Binding

Given the profound difference in ligand-binding properties between isolated SH3 domains of srGAP2 and 4 to constructs that also include the F-BAR and RhoGAP domains, we asked whether polyproline ligand binding to srGAP proteins actually relies on the SH3 domain or is mostly independent of SH3. For this, we separately mutated the two conserved SH3 residues that constitute the Px and xP clefts, tyrosine 781 and tryptophan 765, respectively (Figures 2, 3, and 4). Y781A and W765A substitutes were introduced into 2BRS, expressed and purified under the same conditions (Figure S1), and measured for Robo1-cc3

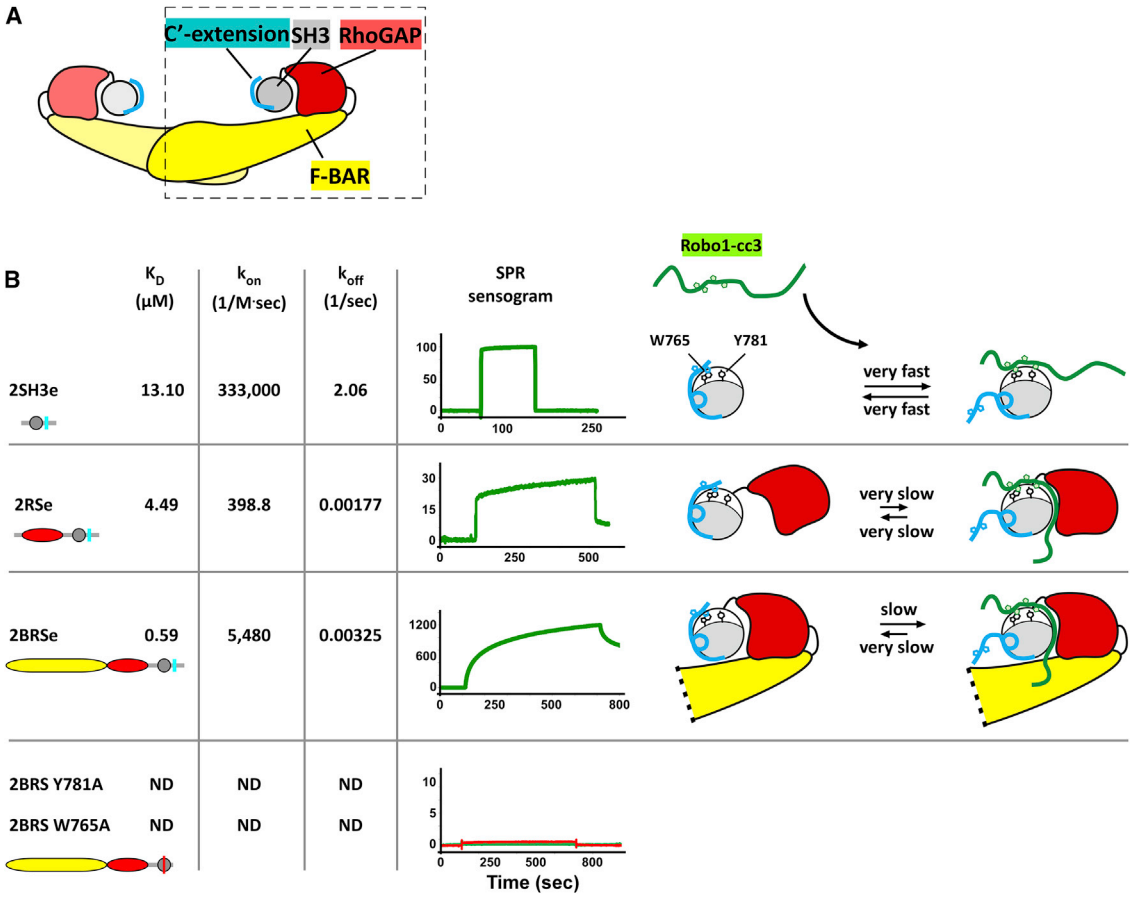


**Figure 4. The F-BAR, RhoGAP, and SH3 Domains Cooperatively Participate in Robo1-cc3 Binding**

(A) Domain organization model for the F-BAR, RhoGAP, and SH3 domains of srGAP2. Each domain is indicated and color coded as in Figure 1A.

(B) A graphical table that describes the mechanism that binds Robo1-cc3 to srGAP2, based on surface plasmon resonance (SPR) kinetic measurements of Robo1-cc3 peptide to the 2SH3e, 2RSe, and 2BRSe srGAP2 constructs. Robo1-cc3 is depicted as a green coil with proline side chains. Weak ligand binding ($K_D$ = 13.1 μM) to the isolated SH3 domain (top), with very fast on- and off-rates, is enhanced by the RhoGAP domain ($K_D$ = 4.49 μM), which may form a composite binding site together with the SH3 domain. Binding is further strengthened by the F-BAR domain ($K_D$ = 0.59 μM), which stabilizes the RhoGAP-SH3 interdomain arrangement, thereby facilitating a faster association rate. It is readily visible from the SPR sensograms (plotted as time versus response units) that very fast Robo1-cc3 association and dissociation rates of 2SH3e are in sharp contrast to the slower rates recorded for 2BRSe and 2RSe. Note that the association with 2RSe is slower than with 2BRSe. Nevertheless, point mutations in the SH3 Px (Y781A) and xP (W765A) pockets abolish the Robo1-cc3 association (bottom panel), thereby demonstrating the essential role of the SH3 domain in Robo1-cc3 binding.

interaction using SPR. In both cases, no interaction was detected (Figure 4). These results show strict dependence on the integrity of the entire SH3 PxxP groove for ligand binding. In conclusion, the PxxP groove of the SH3 domain is probably the most basic element that initiates polyproline binding to srGAP2; however, by itself it can only support weak interactions (Figure 4).

## C′ Extension Eliminates the Binding of a Non-specific Ligand

We have shown that the C′ extension imparts moderate inhibition—up to a 3-fold difference in $K_D$ values—which does not eliminate binding. We next considered what would be the impact of the C′ extension upon binding of polyproline segments that were previously confirmed as not having physiological interactions with srGAP2. Like cc3, cc2 is also a conserved polyproline Robo1 intracellular motif that mediates interactions with several intracellular effectors, but not with srGAPs (Wong et al., 2001). Using MST, we measured and compared the $K_D$ values for a synthesized Robo1-cc2 26-amino-acid peptide (Figure S6) binding to 2BRSe and 2BRS. Under these experimental conditions, we detected no interaction with 2BRSe, while in the absence of the C′ extension (2BRS), cc2 shows binding with an estimated $K_D$ of 41 μM (Table 2 and Figure S7). This experiment points to a potential role of the C′ extension in eliminating srGAP2 interactions with non-specific partners such as Robo1-cc2.

## P807 of the C′ Extension Is the Key for Autoinhibition

After demonstrating that the C′ extension autoinhibits protein binding to srGAP2, we further analyzed the inhibitory mechanism. Based on structure and sequence analyses detailed in the previous sections (Figures 2 and 3), we focused on P807, and tested whether a substitute of P807 will eliminate C′ extension autoinhibition. We noted a missense srGAP3 P823Q

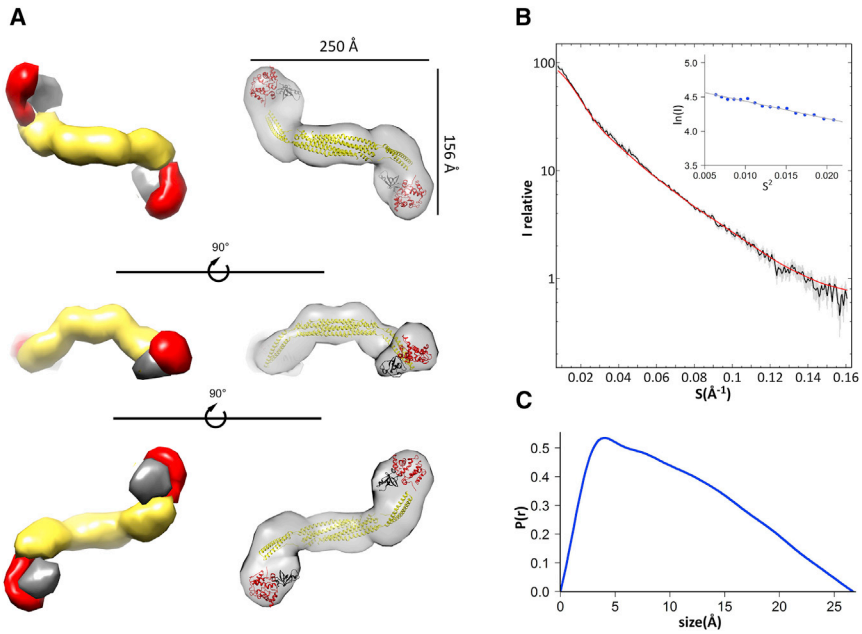


**Figure 5. SAXS 3D Structure and Domain Organization of srGAP4**

(A) SAXS 3D volume of full-length srGAP4 is represented as opaque (left) and transparent (right) envelopes. A 30-Å resolution 3D volume was converted from a bead model and showed two-fold symmetry, with a center reminiscent of other F-BAR structures, and extra densities at the extremities of the volume. The F-BAR domain of PACSIN1 (PDB: 3HAH; in yellow) fitted the center of the volume. Composite RhoGAP-SH3 structures (depicted in red and gray, respectively) were derived from the RhoGAP Beta2-Chimaerin (PDB: 1XA6) and the 2SH3e (this work) crystal structures, and docked to the tip densities.

(B) Superposition of the experimental scattering curve obtained for srGAP4 (black) with the calculated scattering curves derived from the ab initio model of srGAP4 (red). The Guinier plot is shown at the top right.

(C) The *P*(*r*) function of srGAP4 data indicates maximal dimensions ($D_{max}$) of 267 Å.

mutation (srGAP3 P823 exactly aligns with srGAP2 P807, see Figure 2) found in a patient with lung adenocarcinoma (Forbes et al., 2011) and, therefore, chose to substitute srGAP2 P807 with glutamine for our experiments. Expression and purification of 2BRSe P807Q were the same as for the wild-type protein (Figure S1), and the binding affinity of 2BRSe P807Q to Robo1-cc3, Gephyrin, and YLPM1 was measured using MST. In all three cases, 2BRSe P807Q binds with similar or slightly stronger $K_D$ values compared with those measured for 2BRS, which lacks the C′ extension altogether (Table 2; Figures 3 and S7). These results demonstrate the importance of P807 in C′-extension inhibition and show that an xP-mimicry mechanism may be utilized to inhibit polyproline binding.

Interestingly, in three other cases (the NADPH oxidase subunit p47, and the Rlk and Itk non-receptor tyrosine kinases), di-proline motifs juxta-located on carboxy- or amino-flanking regions of SH3 domains mimic polyproline ligands, and thereby block accessibility to the PxxP binding groove (Andreotti et al., 1997; Groemping et al., 2003; Laederach et al., 2003). After observing the mechanistic similarity in SH3 autoinhibition by flanking di-proline motifs, we questioned how common this mode of regulation of SH3 domains might be by analyzing the flanking regions of unique human SH3 sequences with respect to the presence and conservation of di-proline motifs. Our analysis showed that in 49 out of the 209 cases examined, conserved di-proline motifs were found at a range of ±40 amino acids from the SH3 boundaries (List S1), and that in the other 160 cases single conserved prolines and PxxP motifs were common. From this analysis, we conclude that autoinhibition of SH3 domains by means of ligand mimicry may be a general mechanism for eliminating non-specific binding to SH3 domains.

### SAXS Outlines the Structure and Packing of the F-BAR, RhoGAP, and SH3 Domains of Intact srGAP4

We showed that protein binding to SH3 is dramatically enhanced by the F-BAR and RhoGAP domains of both srGAP2 and srGAP4, and hypothesized that this effect is due to a specific intramolecular arrangement of the three domains. To obtain a structural basis that will clarify these observations and hypotheses, we determined the solution structure of full-length srGAP4 using SAXS (small-angle X-ray scattering), and assigned the domain organization by fitting homologous crystal structures. The shape of srGAP4 was determined ab initio, and the model fit the experimental data with a $\chi^2$ discrepancy of 0.83 (Figure 5 and Table 3).

This structure displays a two-fold symmetry, where two srGAP4 protomers are tightly packed together along the long axis of the molecule. Given its sequence similarity to other F-BAR domains, it is not surprising that the core of the srGAP4 structure resembles in size and angular arrangement the canonical helix bundle and extended arms, as seen in the crystal structures of FBP17 and FCHo2 (PDB: 2EFL and 3HAH). At the tips of the F-BAR arms, additional densities that correspond in volume to the RhoGAP and SH3 domains show close interactions to each other and the F-BAR arms, thus supporting our previous analysis of cooperative participation of the three domains in ligand binding.

## DISCUSSION

In this study, we investigated the mechanism of polyproline ligand binding to srGAP2, and discovered two molecular elements that together facilitate higher affinity and greater specificity association than previously known. First, we showed that the SH3 domain of srGAP2 is necessary but not sufficient for effective ligand binding, and that the cooperative participation of the F-BAR and RhoGAP domains provides an approximately 15-fold increase in binding affinity. The second element that modulates srGAP2 associations is an SH3 carboxy extension that occludes a portion of the SH3 PxxP binding groove, thereby restricting access of the binding partners. Finally, depending on the local concentration of srGAP2, the carboxy extension binds

**Table 3. SAXS Statistics**

| Structural Parameters | |
|---|---|
| $R_g$ (Å) (from Guinier) | 87.4 ± 0.86 |
| $D_{max}$ (Å) | 267 |
| Porod volume estimate (Å$^3$) | 400.8 |
| DAMMIN excluded volume (Å$^3$) | 450 |
| **Molecular Mass Determination** | |
| $V_c$ (Å$^2$) | 14.77 |
| $Q_r$ (Å$^3$) | 24.94 |
| SAXS determined mass (kDa) | 203 |
| Theoretical mass (kDa) | 210 |
| Molecular mass $M_r$ (kDa) (from Porod invariant) | 200–250 |

in *cis* or in *trans* to a neighboring srGAP2 molecule. We hypothesize that the transition from the *cis* to *trans* states is triggered by the recruitment of srGAP2 to the plasma membrane, where intermolecular srGAP2 interactions form a membrane-associated lattice.

## The SH3 C′ Extension Is an Autoinhibitory Element for Polyproline Binding to srGAP2

Here, we present structural and biochemical evidence revealing the role of the SH3 carboxy extension (C′ extension) in the autoinhibition of protein binding to srGAP2. The C′ extension eliminates the non-specific binding of the Robo1-cc2 segment, which is not an srGAP2 ligand, and moderately inhibits the binding of the previously confirmed srGAP2 binding partners: Robo1-cc3, Gephyrin, and YLPM1. Our crystallographic studies revealed the structure of the SH3 C′ extension that interacts in *trans* with a symmetry-mate molecule to occupy the SH3 specificity zone and the xP pocket. C′-extension-mediated *trans* interactions also occur in solution, as demonstrated by CG-MALS, with a dimerization dissociation constant of 1.39 mM. SH3 interactions involving the specificity zone are not uncommon and, in several documented cases (Saksela and Permi, 2012), SH3 domains interact with other proteins through expansion of the binding surface from the PxxP groove to secondary SH3 binding surfaces such as the "specificity zone," thereby providing additional specificity and affinity. However, unlike canonical polyproline ligands, in our case the C′ extension does not cover the entire PxxP binding groove but rather the xP cleft alone. This way, the specificity zone seems to serve as a docking site that places the minimal inhibitory element in the exact position to cover the xP binding pocket, providing high specificity with a moderate inhibitory effect. The way in which the C′ extension residues interact with the xP pocket is a typical example of substrate mimicry, in which proline 807 assumes the exact rotamer and spatial positions, as do class I polyproline ligands (Lim et al., 1994), with a hydrogen bond formed between the proline backbone carbonyl and the tryptophan indole amine. The evolutionary conservation of srGAP2 P807 further highlights the functional importance of this residue. The key role of P807 in autoinhibition was demonstrated when the srGAP2 (2BRSe construct) mutant, introduced with a P807Q substitute, abolished the inhibitory activity of the C′ extension in binding Robo1-cc3, Gephyrin, and YLPM1 ligands, and presented $K_D$ values similar to those of the srGAP2 construct (2BRS), which lacks the C′ extension. We also demonstrated that the C′ extension can eliminate the binding of non-specific polyproline segments, as in the case of the Robo1-cc2. cc2 is also a conserved polyproline cytoplasmic motif in Robo receptors that, unlike the cc3 motif, is not involved in Robo1-srGAP2 interaction in cell culture (Wong et al., 2001). While cc2 binds 2BRS with an approximate $K_D$ of 43 μM, no binding to the 2BRSe construct was detected, demonstrating the potential role of the C′ extension in eliminating non-specific interactions to srGAP2.

## The F-BAR, RhoGAP, and SH3 Domains Cooperatively Participate in Polyproline Ligand Binding

The binding affinity of Robo1-cc3, Gephyrin, and YLPM1 peptides to the isolated srGAP2 SH3 domain is relatively weak, with $K_D$ values ranging from 2.5 to 40.9 μM. However, much stronger binding is measured for srGAP2 constructs that also include the F-BAR and RhoGAP domains. Moreover, the binding kinetics, as measured by SPR, is fundamentally different for 2SH3 compared with the 2RS and 2BRS constructs. While Robo1-cc3 binding to the isolated SH3 domain has very fast on- and off-rates, much slower rates were measured for the 2RS and 2BRS constructs. It is noteworthy that while avidity might have been considered as one of the factors contributing to stronger binding in the 2BRS constructs due to its F-BAR-mediated dimeric structure, the 2RS constructs are strictly monomeric and still show much stronger binding than the isolated 2SH3 constructs. In spite of the strong contribution of the F-BAR-RhoGAP domains to the ligand binding, as reflected by the dramatic difference in $K_D$, $k_{on}$, and $k_{off}$ between isolated 2SH3 and 2BRS constructs, point mutations (Y781A and W765A) that target the SH3 Px and xP binding pockets nevertheless abolished the binding, thereby demonstrating that polyproline-srGAP2 interactions rely on the integrity of the SH3 PxxP binding groove.

There are several documented precedents for composite domains that facilitate high-affinity binding by forming a better binding surface. One example is the interaction between the two NADPH oxidase subunits, p47 and p22 (Groemping et al., 2003). There, a polyproline segment of p22 simultaneously binds the PxxP grooves of two consecutive p47 SH3 domains (designated SH3A and SH3B) which, together, form an elaborate binding surface. Similar to the F-BAR-RhoGAP domains of srGAP2, which do not bind Robo1-cc3 independently (deduced from the lack of Robo1-cc3 binding to the Y781A and W765A mutants), SH3B of p47 by itself does not show p22 interaction. On the other hand, dissociation constants of 7 μM for the binding of p22 to SH3A and 0.4 μM for the tandem SH3A and SH3B domains were calculated. These values are strikingly similar to the $K_D$ values of 6.9 and 0.48 μM that we measured, using MST for the binding of Robo1-cc3 to 2SH3 and 2BRS, respectively. Further measurements of Robo1-cc3 to 2RS and 2RSe showed differences in the on- and off-rates in comparison with the 2BRS constructs, and allowed better understanding of the way in which certain polyproline-containing proteins associate with srGAP2.

The 14- or 21-fold difference (for MST and SPR, respectively) in $K_D$ values, and the dramatic differences in the on- and off-rates between 2SH3 and 2BRS, led us to the conclusion that the RhoGAP domain forms a composite ligand-binding surface together with the SH3 domain, and that the role of the F-BAR domain is in stabilizing their relative orientation to each other by

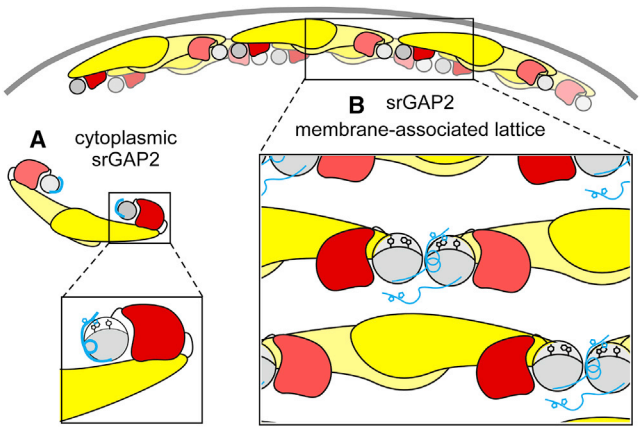


**Figure 6. Proposed Model for a Link between the Subcellular Localization of srGAP2 and C′ Extension *cis* or *trans* Position**

(A) srGAP2 is an F-BAR-mediated dimer that, when localized to the nucleus or cytoplasm, is at a relatively low concentration that does not allow the C′ extension to interact in *trans* with other srGAP2 molecules. The srGAP2 soluble form allows only *cis* interactions, which moderately autoinhibit ligand binding. (B) Upon its activation and recruitment to the membrane surface, srGAP2 forms an F-BAR-mediated oligomeric lattice that brings SH3 domains from neighboring molecules into close proximity, thereby allowing C′ extension interactions in *trans*. There, the C′ extension of a "donor" molecule binds to the neighboring, "acceptor" molecule, while the C′ extension of the acceptor, due to structural constraints, cannot reach the donor, leaving it exposed.

allowing ten times faster on-rate ligand binding than with 2RS. It is interesting that srGAP proteins were initially discovered by a yeast two-hybrid screen against Robo receptors (Wong et al., 2001), while a later screen that used isolated SH3 domains to identify new srGAP-binding partners failed to pick up Robo receptors (Okada et al., 2013). In light of our new knowledge about the auxiliary role of the F-BAR and RhoGAP domains in polyproline binding to the SH3 domain, this apparent discrepancy has been settled. Future screens will be more effective if using larger srGAP constructs when searching for new srGAP-binding partners.

### Autoinhibition in *cis* and Lattice Interactions in *trans*: Two Roles for One Short C′ Extension?

In the crystal structure of 2SH3e, the C′ extension of a donor molecule interacts in *trans* with a symmetry-mate acceptor, while the C′ extension of the acceptor cannot reach the donor's binding site. Instead, the symmetry mate binds another neighboring molecule, and so on. In addition, in solution, CG-MALS measurements showed that the C′ extension mediates the dimerization of 2SH3e with a $K_D$ of 1.39 mM. However, C′-extension interaction in *cis* is also evident, as the binding of polyproline peptides is inhibited by the C′ extension when srGAP2 is in a concentration range of 0.1–30 μM, in which 2SH3e is virtually entirely monomeric in solution. In fact, analysis of the 2SH3e crystal structure shows that it is sterically possible for the C′ extension to reach a *cis* binding position, at the expense of several atomic contacts that exist in the *trans* conformation. These results and analyses draw a picture in which *trans* interactions occur under high local concentrations, while interactions in *cis* occur at lower srGAP2 concentrations. We attribute these high and low concentrations and the corresponding *trans* and *cis* C′-extension positions to actual physiological conditions in the course of srGAP protein activity.

The F-BAR domain of srGAP2 binds to and reshapes plasma membranes to form filopodia-like protrusions (Guerrier et al., 2009). Judging from the uniform diameter and shape of these protrusions and based on our current knowledge of how BAR domains deform membranes (Frost et al., 2009), we posit that the srGAP2 F-BAR domains form oligomeric lattices on membrane surfaces that are held by lateral and tip-to-tip interactions (Figure 6). Of special relevance to our case is the full-length cryoelectron-microscopic structure of endophilin in its membrane-bound lattice form, as determined by Mim et al. (2012), who depict how SH3 domains of neighboring molecules dimerize at the proximal points of the N-BAR domain tips. A very high (3–5 mM), effective concentration and the accurate positioning of the interacting domains are thought to drive SH3 dimerization, thereby contributing to the formation and stability of the endophilin lattice. Similarly, we hypothesize that SH3 domains of neighboring membrane-bound srGAP2 molecules are placed in close proximity to each other, bringing about a high, effective concentration that exceeds the 2SH3e 1.39-mM dimerization constant. Such proximity may promote the C′ extensions to form *trans* interactions with a neighboring molecule at the expense of the weaker *cis* contacts. The observation made by Guerrier et al. (2009) that tryptophan 765 (the SH3 docking site for the C′ extension) is critical for srGAP2 filopodia-like formation in COS-7 cells may reflect a vital role for C′-extension-mediated intermolecular interactions in the membrane-associated srGAP2 lattice.

## Conclusions

In this study, we show that the F-BAR and RhoGAP domains participate in cooperative ligand binding to the SH3 domains of srGAP2 and srGAP4. The dramatic differences in $K_D$, $k_{on}$, and $k_{off}$ indicate that the RhoGAP and SH3 domains form a composite surface that binds polyproline segments better than the isolated SH3 domain, and that the F-BAR domain stabilizes this surface. We also show that protein binding to srGAP2 is inhibited by an SH3-carboxy extension (C′ extension) that interacts with the specificity zone and xP cleft of the SH3 domain, and has the capability of eliminating the binding of the non-specific, Robo1-cc2 polyproline segment. At high srGAP2 concentrations, the C′ extension binds in *trans* to another srGAP2 molecule ($K_D$ = 1.39 mM). We hypothesize that the *trans* position reflects a second role that the SH3 domain fulfills in the context of membrane-associated srGAP2, where SH3-SH3 lateral interactions contribute to the stability and structure of the, primarily F-BAR-mediated, lattice.

## EXPERIMENTAL PROCEDURES

### Crystallization, Data Collection, and Structure Determination

Purified 2SH3e was screened for crystallization using the commercial screens CrystalScreen HT, PegRx HT, and SaltRx HT (Hampton Research), in 96-well hanging-drop clear polystyrene microplates (Corning Life Sciences) at 4°, 12°, and 20°C, respectively. A 1:1 sample/reservoir ratio was used, with a final drop size of 0.3 μl. Eight weeks after setup, a single crystal hit appeared at 4°C in 2.0 M ammonium sulfate. The crystallization condition was further refined using 24-well hanging-drop vapor-diffusion plates by varying pH values and precipitant and protein concentrations. Best diffracting crystals were obtained when the protein concentration was 19 mg/ml, with a reservoir content of

2.35 M ammonium sulfate and 0.1 M MES (pH 6.25) at 4°C. Crystals appeared after about 8 weeks in 2-μl drops (protein/reservoir ratio of 1:1), and were harvested 4 weeks after appearance. The crystals were cryoprotected by adding 13.5% glycerol to the mother liquor solution before harvesting, and flash-frozen in liquid nitrogen.

Diffraction data for the 2SH3e crystals were measured on beamlines ID23-1 (Nurizzo et al., 2006) and ID29 (de Sanctis et al., 2012) at the ESRF and ID14.1 (Mueller et al., 2012) at BESSY II, and were processed and scaled using the XDSAPP software package (Krug et al., 2012). Molecular replacement and initial model building were carried out using the BALBES server (Long et al., 2008), which placed the two 2SH3e molecules in the asymmetric unit. Further manual model building and refinement were performed using Coot (Emsley et al., 2010), Phenix-refine (Adams et al., 2010; Afonine et al., 2012), and the ReDo server (Joosten et al., 2012). Data collection and refinement statistics are summarized in Table 1.

### BioSAXS Analysis

SAXS experiments were conducted at the ESRF BM29 beamline, where an on-line high-performance liquid chromatography system (Viscotek GPCmax; Malvern Instruments) was attached directly to the sample-inlet valve of the sample changer. srGAP4 samples at a concentration range of 0.5–5 mg/ml were loaded into vials and automatically injected into the column (Superdex 200 10/300 GI; GE Healthcare) via an integrated syringe system. Prior to each run, the column was equilibrated with 1.5-column volumes of buffer (25 mM phosphate buffer [pH 8], 200 mM NaCl, and 1 mM DTT), and the baseline was monitored. All data were collected at a wavelength of 0.9919 Å using a sample-to-detector (PILATUS 1M; Dectris) distance of 2.81 m, corresponding to an s range of 0.08–4.5 nm. Approximately 3,600 frames (1 frame per second) were collected per 60-min sample run. Initial data processing was performed automatically using the EDNA pipeline, generating radially integrated, calibrated, and normalized one-dimensional profiles for each frame. All frames were compared with the initial frame, and matching frames were merged to create the reference buffer. Any subsequent frames that differed from the reference buffer were subtracted and then processed within the EDNA pipeline. The invariants calculated by the ATSAS tool (AUTORG) were used to select a subset of frames from the peak scattering intensity. Frames with a consistent $R_g$ from the peak scattering intensity were merged to yield a single-averaged frame corresponding to the scattering of an individual size-exclusion chromatography-purified species.

The averaged scattering data were further evaluated using PRIMUS. The isotropic scattering intensity $I(q)$ was transformed to the distance distribution function $P(r)$ using the program GNOM, which was also used to calculate the particle maximum dimensions $D_{max}$. $D_{max}$ was considered to be optimal when the $R_g$ obtained from the $P(r)$ plot was equal to that obtained from the Guinier analysis. For ab initio modeling of the SAXS data, 20 sets of independent models were calculated using DAMMIN applying two-fold symmetry, then averaged and aligned using DAMAVER. Molecular masses were determined as described by Rambo and Tainer (2013).

## SUPPLEMENTAL INFORMATION

Supplemental Information includes Supplemental Experimental Procedures, seven figures, and one list and can be found with this article online at http://dx.doi.org/10.1016/j.str.2015.08.009.

## ACKNOWLEDGMENTS

This paper is dedicated to the memory of the late Dr. Felix Frolow, a pioneer of cryocrystallography. The authors thank Alexander Varvak, Ilana Lebenthal, Eitan Lerner, Sivan Shemesh, and Sharon Victor of Bar-Ilan University. Thanks are extended to the staff of beamlines BM29, ID23, and ID29 of ESRF, and the staff of BESSY II BL14.1. This work was supported by funds from the ISF (grant no. 182/10, to Y.O.) and BSF (grant no. 2013310, to Y.O.).

Received: March 22, 2015
Revised: August 16, 2015
Accepted: August 17, 2015
Published: September 10, 2015

## REFERENCES

Adams, P.D., Afonine, P.V., Bunkoczi, G., Chen, V.B., Davis, I.W., Echols, N., Headd, J.J., Hung, L.W., Kapral, G.J., Grosse-Kunstleve, R.W., et al. (2010). PHENIX: a comprehensive Python-based system for macromolecular structure solution. Acta Crystallogr. D Biol. Crystallogr. *66*, 213–221.

Afonine, P.V., Grosse-Kunstleve, R.W., Echols, N., Headd, J.J., Moriarty, N.W., Mustyakimov, M., Terwilliger, T.C., Urzhumtsev, A., Zwart, P.H., and Adams, P.D. (2012). Towards automated crystallographic structure refinement with phenix.refine. Acta Crystallogr. D Biol. Crystallogr. *68*, 352–367.

Andreotti, A.H., Bunnell, S.C., Feng, S., Berg, L.J., and Schreiber, S.L. (1997). Regulatory intramolecular association in a tyrosine kinase of the Tec family. Nature *385*, 93–97.

Carlson, B.R., Lloyd, K.E., Kruszewski, A., Kim, I.H., Rodriguiz, R.M., Heindel, C., Faytell, M., Dudek, S.M., Wetsel, W.C., and Soderling, S.H. (2011). WRP/srGAP3 facilitates the initiation of spine development by an inverse F-BAR domain, and its loss impairs long-term memory. J. Neurosci. *31*, 2447–2460.

Coutinho-Budd, J., Ghukasyan, V., Zylka, M.J., and Polleux, F. (2012). The F-BAR domains from srGAP1, srGAP2 and srGAP3 regulate membrane deformation differently. J. Cell Sci. *125*, 3390–3401.

de Sanctis, D., Beteva, A., Caserotto, H., Dobias, F., Gabadinho, J., Giraud, T., Gobbo, A., Guijarro, M., Lentini, M., Lavault, B., et al. (2012). ID29: a high-intensity highly automated ESRF beamline for macromolecular crystallography experiments exploiting anomalous scattering. J. Synchrotron Radiat. *19*, 455–461.

Emsley, P., Lohkamp, B., Scott, W.G., and Cowtan, K. (2010). Features and development of Coot. Acta Crystallogr. D Biol. Crystallogr. *66*, 486–501.

Endris, V., Haussmann, L., Buss, E., Bacon, C., Bartsch, D., and Rappold, G. (2011). SrGAP3 interacts with lamellipodin at the cell membrane and regulates Rac-dependent cellular protrusions. J. Cell Sci. *124*, 3941–3955.

Forbes, S.A., Bindal, N., Bamford, S., Cole, C., Kok, C.Y., Beare, D., Jia, M., Shepherd, R., Leung, K., Menzies, A., et al. (2011). COSMIC: mining complete cancer genomes in the Catalogue of Somatic Mutations in Cancer. Nucleic Acids Res. *39*, D945–D950.

Frost, A., Unger, V.M., and De Camilli, P. (2009). The BAR domain superfamily: membrane-molding macromolecules. Cell *137*, 191–196.

Greenfield, N.J. (2006). Using circular dichroism spectra to estimate protein secondary structure. Nat. Protoc. *1*, 2876–2890.

Groemping, Y., Lapouge, K., Smerdon, S.J., and Rittinger, K. (2003). Molecular basis of phosphorylation-induced activation of the NADPH oxidase. Cell *113*, 343–355.

Guerrier, S., Coutinho-Budd, J., Sassa, T., Gresset, A., Jordan, N.V., Chen, K., Jin, W.L., Frost, A., and Polleux, F. (2009). The F-BAR domain of srGAP2 induces membrane protrusions required for neuronal migration and morphogenesis. Cell *138*, 990–1004.

Joosten, R.P., Joosten, K., Murshudov, G.N., and Perrakis, A. (2012). PDB_REDO: constructive validation, more than just looking for errors. Acta Crystallogr. D Biol. Crystallogr. *68*, 13.

Krug, M., Weiss, M.S., Heinemann, U., and Mueller, U. (2012). XDSAPP: a graphical user interface for the convenient processing of diffraction data using XDS. J. Appl. Crystallogr. *45*, 5.

Laederach, A., Cradic, K.W., Fulton, D.B., and Andreotti, A.H. (2003). Determinants of intra versus intermolecular self-association within the regulatory domains of Rlk and Itk. J. Mol. Biol. *329*, 1011–1020.

Li, X., Chen, Y., Liu, Y., Gao, J., Gao, F., Bartlam, M., Wu, J.Y., and Rao, Z. (2006). Structural basis of Robo proline-rich motif recognition by the srGAP1 Src homology 3 domain in the Slit-Robo signaling pathway. J. Biol. Chem. *281*, 28430–28437.

Lim, W.A., Richards, F.M., and Fox, R.O. (1994). Structural determinants of peptide-binding orientation and of sequence specificity in SH3 domains. Nature *372*, 375–379.

Long, F., Vagin, A.A., Young, P., and Murshudov, G.N. (2008). BALBES: a molecular-replacement pipeline. Acta Crystallogr. D Biol. Crystallogr. *64*, 125–132.

Mason, F.M., Heimsath, E.G., Higgs, H.N., and Soderling, S.H. (2011). Bimodal regulation of a formin by srGAP2. J. Biol. Chem. *286*, 6577–6586.

Mim, C., Cui, H., Gawronski-Salerno, J.A., Frost, A., Lyman, E., Voth, G.A., and Unger, V.M. (2012). Structural basis of membrane bending by the N-BAR protein endophilin. Cell *149*, 137–145.

Mueller, U., Darowski, N., Fuchs, M.R., Förster, R., Hellmig, M., Paithankar, K.S., Pühringer, S., Steffien, M., Zocher, G., and Weiss, M.S. (2012). Facilities for macromolecular crystallography at the Helmholtz-Zentrum Berlin. J. Synchrotron Radiat. *19*, 8.

Nurizzo, D., Mairs, T., Guijarro, M., Rey, V., Meyer, J., Fajardo, P., Chavanne, J., Biasci, J.-C., McSweeney, S., and Mitchell, E. (2006). The ID23-1 structural biology beamline at the ESRF. J. Synchrotron Radiat. *13*, 17.

Okada, H., Uezu, A., Mason, F.M., Soderblom, E.J., Moseley, M.A., 3rd, and Soderling, S.H. (2013). SH3 domain-based phototrapping in living cells reveals Rho family GAP signaling complexes. Sci. Signal. *4*, rs13.

Opatowsky, Y., Chen, C.C., Campbell, K.P., and Hirsch, J.A. (2004). Structural analysis of the voltage-dependent calcium channel beta subunit functional core and its complex with the alpha 1 interaction domain. Neuron *42*, 387–399.

Qualmann, B., Koch, D., and Kessels, M.M. (2011). Let's go bananas: revisiting the endocytic BAR code. EMBO J. *30*, 3501–3515.

Rambo, R.P., and Tainer, J.A. (2013). Accurate assessment of mass, models and resolution by small-angle scattering. Nature *496*, 477–481.

Saksela, K., and Permi, P. (2012). SH3 domain ligand binding: what's the consensus and where's the specificity? FEBS Lett. *586*, 2609–2614.

Soderling, S.H., Guire, E.S., Kaech, S., White, J., Zhang, F., Schutz, K., Langeberg, L.K., Banker, G., Raber, J., and Scott, J.D. (2007). A WAVE-1 and WRP signaling complex regulates spine density, synaptic plasticity, and memory. J. Neurosci. *27*, 355–365.

Wong, K., Ren, X.R., Huang, Y.Z., Xie, Y., Liu, G., Saito, H., Tang, H., Wen, L., Brady-Kalnay, S.M., Mei, L., et al. (2001). Signal transduction in neuronal migration: roles of GTPase activating proteins and the small GTPase Cdc42 in the Slit-Robo pathway. Cell *107*, 209–221.

Yamazaki, D., Itoh, T., Miki, H., and Takenawa, T. (2013). srGAP1 regulates lamellipodial dynamics and cell migratory behavior by modulating Rac1 activity. Mol. Biol. Cell *24*, 3393–3405.

Yao, Q., Jin, W.L., Wang, Y., and Ju, G. (2008). Regulated shuttling of Slit-Robo-GTPase activating proteins between nucleus and cytoplasm during brain development. Cell Mol. Neurobiol. *28*, 205–221.

Zarrinpar, A., Bhattacharyya, R.P., and Lim, W.A. (2003). The structure and function of proline recognition domains. Sci. STKE *2003*, RE8.

 